Computer Modeling in
Engineering & Sciences

Tech Science Press

https://doi.org/10.32604/cmes.2026.086863

ARTICLE

Thermal Transport and Physics-Guided Optimization of MHD Buongiorno Nanofluid over a Porous Cylinder with Machine Learning Applications

Hameed Ullah Khan[1], Muhammad Naveed Khan[2,*], N. Ameer Ahammad[3], Nurul Amira Zainal[4,*], Shahzad Sarwar[5], Muhammad Imran Khan[1] and Afef Dhahbi[6]

[1]Department of Mathematics & Statistics, International Islamic University, Islamabad, Pakistan
[2]School of Aeronautics and Astronautics, Zhejiang University, Hangzhou, Zhejiang, 310027, China
[3]Department of Mathematics, Faculty of Science, University of Tabuk, P.O. Box 741, Tabuk, 71491, Saudi Arabia
[4]Fakulti Teknologi dan Kejuruteraan Mekanikal, Universiti Teknikal Malaysia Melaka, Hang Tuah Jaya, 76100, Durian Tunggal, Melaka, Malaysia
[5]Department of Mathematics, King Fahd University of Petroleum and Minerals (KFUPM), Dhahran, 31261, Saudi Arabia
[6]Department of Financial and Accounting Management Programs, Applied College Princess Nourah bint Abdulrahman University, P.O. Box 84428, Riyadh, 11671, Saudi Arabia

*Corresponding Authors: Muhammad Naveed Khan. Email: mnkhan@zju.edu.cn;
Nurul Amira Zainal. Email: nurulamira@utem.edu.my

Received: 09 June 2026; Accepted: 30 July 2026; Published: 28 August 2026

ABSTRACT: The thermal and solutal transport mechanisms in non-Newtonian fluids play a substantial role in energy systems, thermal management, polymer processing, and biomedical engineering. In this study, an integrated Local Non-Similarity Physics-Informed Neural Network framework is developed to investigate the non-similar boundary layer flow, heat, and mass transport of Williamson nanofluid through a horizontal porous cylinder under the combined effects of magnetohydrodynamics and porous media. The leading nonlinear system of equations that represents the problem is transformed into a coupled ordinary differential equation using the local non-similarity method. The resulting system is solved using a Physics guided Neural Network implemented in PyTorch, where the foremost equations and boundary conditions are incorporated into a physics-based loss function without requiring labeled training data. The influences of the magnetic parameter (M), surface heating parameter (γ), Prandtl number (Pr), Schmidt number (Sc), Brownian motion parameter (N_b), and thermophoretic parameter (N_t) on the velocity, temperature, concentration, skin friction coefficient, local Nusselt number and local Sherwood number are systematically investigated. The PINN predictions show excellent agreement with benchmark numerical solutions obtained using the Scipy boundary value solver, while maintaining low L^2 errors, confirming the accuracy and robustness of the proposed framework. The results demonstrate that the LNS-PINN approach provides an efficient and reliable mesh-free computational methodology for solving highly nonlinear non-similar transport problems involving coupled heat and mass transfer in non-Newtonian nanofluids.

KEYWORDS: Thermal and solutal features; buongiorno nanofluid; Williamson fluid; machine learning algorithm; thermal radiation

1 Introduction

Artificial Intelligence is the domain of developing and designing computers and robots that are capable of behaving in ways that both mimic and go beyond human capabilities. AI-enabled applications can contextualize and analyze data to produce information or initiate actions on their own without human intervention. Artificial intelligence is a bigger domain within which various machine learning algorithms work. This subdivision of AI uses algorithms to automatically learn insights and recognize patterns from data, applying that learning to make increasingly better decisions. Machine learning has a broad range of applications, including prognostication, optimization, pattern and speech recognition, and image processing [1]. A Neural network is an artificial intelligence-based model that is inspired by the brain's structure and operation. It possesses enormous applications in many sectors, such as computational materials and chemical sciences, biomedical sciences, climate forecasting and aerospace and mechanical engineering. A neural network is one of the main machine learning models used for supervised learning, where input data is transformed into associated outputs. Training is done by using a particular set of input and output data, where the neural network parameters are adjusted such that the differences between the actual and predicted values are minimized. The method of convergence is through the optimization of a loss function, usually quantified by Mean Square Error (MSE). This optimization process relies on gradient-based algorithms with automatic differentiation for the efficient performance of backpropagation [2].

PINNs have recently become a favorable alternative for addressing boundary layer flow and heat transfer issues. In contrast to data-driven machine learning models, PINNs embed the governing partial differential equations, boundary conditions, and physical constraints directly in the loss function of deep neural networks. By applying governing-equation residuals at collocation points, PINNs attain mesh-free approximations capable of capturing the underlying physical response with high accuracy. Applications of PINNs to boundary layer flows are of great interest in simulating velocity and temperature fields under diverse flow regimes. They have successfully modeled magnetohydrodynamic boundary layers, porous media convective heat transfer, nanofluid transport, and non-Newtonian fluid flow. Additionally, PINNs provide accurate predictions of engineering quantities of interest, i.e., skin friction coefficients and Nusselt numbers, while minimizing computational overhead over classical solvers.

PINNs have emerged as a prominent topic in scientific machine learning, offering a hybrid approach that integrates physics-based modeling within a deep learning framework [3]. This approach has been successfully applied to a range of problems in fluid mechanics [4] and heat transfer [5]. Recent studies have increasingly concentrated on employing neural networks to approximate solutions of D.Es [6,7], and Galerkin-based neural networks [8] are prominent unsupervised approaches developed in this domain. These techniques are now commonly used in scientific machine learning, providing a framework that combines physical principles with data-driven inference effortlessly. Despite their promise, the robustness of PINNs across various problem types continues to be a subject of active investigation. PINN techniques and machine learning algorithms have been widely used for solving fluid flow and heat transfer issues. Arzani et al. [9] proposed theory-guided PINNs to improve the accuracy of singularly perturbed boundary layer problems, while Gie et al. [10] developed a singular layer PINN framework for convection-dominated two-dimensional flows. More recently, Cong et al. [11] introduced physics-guided derivative networks to efficiently solve forward free convective boundary layer problems, demonstrating improved prediction accuracy and computational performance.

In engineering, cylindrical shapes are frequently utilized in constructions that are subject to aerodynamic forces in real-world settings, such as bridge cables, chimneys, masts, and pipelines. Cylindrical sections are used in rocket bodies, airplane fuselages, and engine parts in aerospace and automotive engineering, where precise pressure drag and heat load prediction are essential for effective design and operation. One of the most addressed canonical issues in fluid mechanics is the flow past a circular cylinder, which offers important insights into phenomena including drag forces, vortex shedding, and boundary layer separation [12,13]. Extensive research has been carried out on the boundary layer behavior of non-Newtonian fluids in recent years [14–17]. Recently, PINNs have emerged as a powerful mesh-free computational framework for solving complex fluid flow and heat transfer problems governed by nonlinear differential equations.

Ref. [18] introduced a PINN-based immersed boundary method for incompressible flows, while Ref. [19] demonstrated the applicability of PINNs to low Reynolds-number flow over a cylinder. Further developments include the integration of PINNs architecture for flow field reconstruction and prediction [20], and the extension of PINNs to incompressible flows with moving boundaries was analyzed [21]. Ref. [22] applied PINNs to transonic flow around a cylinder at high Reynolds numbers, illustrating their capability for complex aerodynamic simulations. More recently, Ref. [23] employed PINNs to investigate heat transfer in non-Newtonian Casson fluid flow around a horizontal cylinder. These studies demonstrate the growing success of physics-informed deep learning in computational fluid dynamics. However, the application of PINNs to non-similar Williamson nanofluid flow through a horizontal cylinder using the LNS approach together with coupled heat and mass transfer in porous media remains largely unexplored, thereby motivating the present investigation.

The present work develops an integrated computational framework that combines the LNS method with PINN to investigate the non-similar nanofluid flow of a Williamson nanofluid over a horizontal cylinder. Furthermore while Ref. [24] primarily focused on the numerical solution of the governing equations, the present work demonstrates the applicability of the proposed LNS-PINN framework to accurately solve the nonlinear truncated system of ordinary differential equations (ODEs), validates the predictions against the SciPy boundary value solver and performs a comprehensive parametric investigation of the magnetic parameter, convective heating factor, Brownian motion and thermophoresis on the velocity, temperature, concentration. The contribution of this study is not merely the application of PINN, but the extension of the LNS formulation into a robust physics-informed deep learning framework for solving highly nonlinear, coupled non-similar transport problems involving Williamson nanofluids with multiple interacting physical mechanisms.

2 Mathematical Modeling

From the domain of fluid mechanics, we consider a steady, incompressible magnetohydrodynamic (MHD) Williamson non-Newtonian flow with corresponding heat and mass transfer over a horizontal cylinder of radius a. The physical configuration is illustrated schematically in Fig. 1. The angular coordinate is defined as: $\Phi = \frac{x}{a}$, $0 \leq \Phi \leq \pi$, where the buoyancy force components are projected along the tangential direction. It is assumed that the surface temperature and concentration of the cylinder are higher than the ambient fluid values, i.e., $T_w > T_\infty$ and $C_w > C_\infty$. The magnetic field induced by the flow is neglected because the magnetic Reynolds number is small ($Re_m \ll 1$), and the Hall current effect is ignored because the Hall parameter is assumed to be sufficiently small under the present flow conditions. Using the boundary layer approximations, the governing equations take the following form [24]:

$$\frac{\partial u}{\partial x} + \frac{\partial v}{\partial y} = 0 \tag{1}$$

$$u\frac{\partial u}{\partial x} + v\frac{\partial u}{\partial y} = \nu\frac{\partial^2 u}{\partial y^2} + \sqrt{2}\nu\Gamma\frac{\partial u}{\partial y}\frac{\partial^2 u}{\partial y^2} - \frac{\sigma B_0^2}{\rho}u - \frac{\nu}{K}u - cu^2 + g\beta_T\left(T - T_\infty\right)\sin\left(\frac{x}{a}\right) + g\beta_C\left(C - C_\infty\right)\sin\left(\frac{x}{a}\right) \tag{2}$$

$$u\frac{\partial T}{\partial x} + v\frac{\partial T}{\partial y} = \alpha\frac{\partial^2 T}{\partial y^2} - \frac{\partial q_r}{\partial y} + \tau\left[D_B\frac{\partial C}{\partial y}\frac{\partial T}{\partial y} + \frac{D_T}{T_\infty}\left(\frac{\partial T}{\partial y}\right)^2\right] + \frac{\mu}{\rho c_p}\left(\frac{\partial u}{\partial y}\right)^2 \tag{3}$$

$$u\frac{\partial C}{\partial x} + v\frac{\partial C}{\partial y} = D_B\frac{\partial^2 C}{\partial y^2} + \frac{D_T}{T_\infty}\frac{\partial^2 T}{\partial y^2} - K_1(C - C_\infty) \tag{4}$$

whereas thermal radiation is denoted by;

$$\frac{\partial q_r}{\partial y} = -\frac{16\sigma^* T_\infty^3}{3k^*}\left(\frac{\partial^2 T}{\partial y^2}\right)$$

Boundary conditions are as follow

$$u = 0, v = 0, -k\frac{\partial T}{\partial y} = h_w(T_w - T), C = C_w \; at \; y = 0, \tag{5}$$

$$as y \to \infty, u \to 0, v \to 0, T \to T_\infty, C \to C_\infty.$$

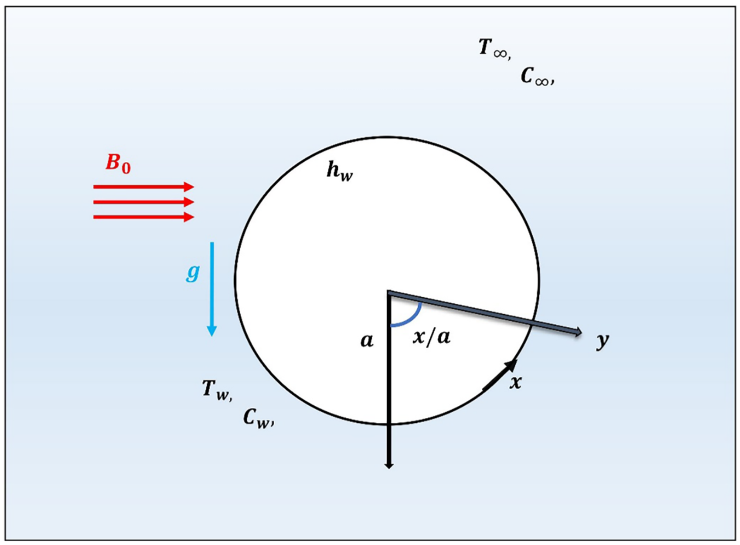

Figure 1: Flow geometry.

The boundary conditions are prescribed as follows: at the cylinder surface $y = 0$, the no-slip and no-penetration conditions $u = 0$, $v = 0$ represent fluid adherence to the solid boundary. A convective thermal boundary condition is applied to the cylinder surface and the surrounding fluid, while a fixed surface concentration represents controlled species injection. Far from the surface $y \to \infty$, the velocity decays to zero and temperature and concentration approach their ambient values, indicating that the boundary layer effects vanish and the fluid remains undisturbed. These boundary conditions are physically consistent with natural convection flow over an infinite horizontal cylinder.

Stream function ψ is defined by $u = \frac{\partial \psi}{\partial y}$ and $v = -\frac{\partial \psi}{\partial x}$. The dimensionless variables are then introduced as follows:

$$f(\xi, \eta) = \frac{\psi}{\nu \xi \sqrt[4]{Gr}}, \xi = \frac{x}{a}, \eta = \frac{y}{a}\sqrt[4]{Gr}, \theta(\xi, \eta) = \frac{T - T_\infty}{T_w - T_\infty}, \phi(\xi, \eta) = \frac{C - C_\infty}{C_w - C_\infty} \tag{6}$$

$$Gr = \frac{g\beta(Tw - T_\infty)a^3}{\nu^2}$$

Applying non-similarity transformation, Eq. (1), i.e., continuity equation satisfied identically, however of Eqs. (2) and (3) are reduced as

$$f''' + ff'' + Wef''f''' - (1 + \xi\Lambda) f'^2 + \frac{sin\xi}{\xi}[\theta + N\phi] - \left(M + \frac{1}{Da}\right) f' = \xi\left(f'\frac{\partial f'}{\partial \xi} - f''\frac{\partial f}{\partial \xi}\right) \tag{7}$$

$$\frac{1}{pr}\left[1 + \frac{4}{3}Rd\right]\theta'' + f\theta' + N_t(\theta')^2 + N_b\theta'\phi' + Ec(f'')^2 = \xi\left(f'\frac{\partial \theta}{\partial \xi} - \theta'\frac{\partial f}{\partial \xi}\right) \tag{8}$$

$$\phi'' + \frac{N_t}{N_b}\theta'' + Scf\phi' - ScK_r\phi = Sc\xi\left(f'\frac{\partial \phi}{\partial \xi} - \phi'\frac{\partial f}{\partial \xi}\right) \tag{9}$$

$$f' = 0, \theta = 1 + \frac{\theta'}{\gamma}, f = 0, \phi = 1 \text{ At } \eta = 0, f' \to 0, \theta \to 0, \phi \to 0 \text{ as } \eta \to \infty \tag{10}$$

The physical parameters appearing in Eqs. (7)–(9) are defined below

$$M = \frac{{B_0}_0^2 a^3}{v_f\sqrt{Gr}}, \quad Pr = \frac{v}{\alpha}, \quad Da = \frac{K\sqrt{Gr}}{a^2}, \quad \Lambda = ca, \quad Rd = \frac{4\sigma^* T_\infty^3}{k^* k},$$

$$We = \frac{\sqrt{2}v\Gamma\xi Gr^{\frac{3}{4}}}{a^2}, \quad N = \frac{\beta_C(C_w - C_\infty)}{\beta_T(T_w - T_\infty)}, \quad K_r = \frac{K_1 a^2}{vGr^{\frac{1}{2}}}, \quad \text{and} \quad Gr = \frac{g\beta(Tw - T_\infty)a^3}{v^2},$$

$$N_b = \frac{\tau D_B(C_w - C_\infty)}{v}, \quad N_t = \frac{\tau D_T \Delta T}{vT_\infty}, \quad Ec = \frac{U^2}{c_p\Delta T}$$

Physical quantities, i.e., C_f, Nu and Sh, are presented below

$$Gr^{-\frac{3}{4}}C_f = \xi f''(\xi, 0) + \frac{We}{2}\xi(f''(\xi, 0))^2 \tag{11}$$

$$NuGr^{-\frac{1}{4}} = -\theta'(\xi, 0) \tag{12}$$

$$ShGr^{-\frac{1}{4}} = -\phi'(\xi, 0) \tag{13}$$

3 Local Non-Similarity Method (LNS)

The LNS technique is a very useful analytical methodology for solving boundary layer flow problems where complete similarity cannot be achieved. In contrast to the similarity method, which involves strong simplifying assumptions, the LNS technique explicitly includes the influence of non-similar terms in the governing boundary layer equations. This is done by adding more dependent variables that capture the streamwise variations, and thereby the original non-similar partial differential equations (PDEs) are approximated using a truncated system of coupled ODEs [25,26].

3.1 First Order Truncation

Under 1st-order truncation approximation, terms on right side of Eqs. (7)–(10) are neglected assuming that $\xi\frac{\partial()}{\partial\xi}$ is insignificant. For $\xi << 1$, we reduce the developed Eqs. (7)–(10) as follows

$$f''' + ff'' + Wef''f''' - (1 + \xi\Lambda) f'^2 - \left(M + \frac{1}{Da}\right) f' + \frac{sin\xi}{\xi}[\theta + N\phi] = 0 \tag{14}$$

$$\frac{1}{pr}\left[1 + \frac{4}{3}Rd\right]\theta'' + f\theta' + N_b\theta'\phi' + N_t(\theta')^2 + Ec(f'')^2 = 0 \tag{15}$$

$$\phi'' + \frac{N_t}{N_b}\theta'' + Scf\phi' - ScK_r\phi = 0 \tag{16}$$

Dimensionless boundary conditions are obtained as follow

$$\text{At } \eta = 0, \quad f' = 0, \quad f = 0, \quad \theta = 1 + \frac{\theta'}{\gamma}, \quad \phi = 1, \quad \eta \to \infty, \quad f' \to 0, \quad \theta \to 0, \quad \phi \to 0 \tag{17}$$

3.2 Second Order Truncation

For second order truncated solution, we considered following terms

$$g = \frac{\partial f}{\partial \xi}, \quad h = \frac{\partial g}{\partial \xi}, \quad \Phi = \frac{\partial \theta}{\partial \xi}, \quad \chi = \frac{\partial \phi}{\partial \xi} \tag{18}$$

Now, we develop equations for g, Φ χ as follow

$$f''' + ff'' + Wef''f''' - (1 + \xi\Lambda) f'^2 - \left(M + \frac{1}{Da}\right) f' + \frac{sin\xi}{\xi}[\theta + N\phi] = \xi (f'g' - f''g) \tag{19}$$

$$\frac{1}{pr}\left[1 + \frac{4}{3}Rd\right]\theta'' + f\theta' + N_b\theta'\phi' + N_t(\theta')^2 + Ec(f'')^2 = \xi (f'\Phi - \theta'g) \tag{20}$$

$$\phi'' + \frac{N_t}{N_b}\theta'' + Scf\phi' - ScK_r\phi = Sc\xi (f'\chi - \phi'g) \tag{21}$$

$$\begin{aligned} &g''' + 2f''g - \Lambda f' + We(g''f''' + f''g''') + fg'' - 2(1 + \xi\Lambda) f'g' - \left(M + \frac{1}{Da}\right) g' \\ &\quad + \left[\left(\frac{sin\xi}{\xi}(\Phi + N\chi)\right) + \left(\frac{\xi\cos(\xi) - \sin(\xi)}{\xi^2}\right)(\theta + N\phi)\right] - f'g' = \xi (g'g' - g''g) \end{aligned} \tag{22}$$

$$\frac{1}{pr}\left[1 + \frac{4}{3}Rd\right]\Phi'' + f\Phi' + 2g\Phi' - f'\Phi + N_b(\Phi'\phi' + \theta'\chi') + 2N_t\theta'\Phi' + 2Ecf''g'' = \xi (g'\Phi - \theta'g) \tag{23}$$

$$\chi'' + \frac{N_t}{N_b}\Phi'' - Sc(K_r\chi + 2g\phi' + f\chi' - f'\chi) = Sc\xi(f'\chi - \phi'g) \tag{24}$$

$$\begin{aligned} &\text{At } \eta = 0, \quad f' = 0, \quad f = 0, \quad \theta = 1 + \tfrac{\theta'}{\gamma}, \quad \phi = 1, \quad g' = 0, \quad g = 0, \quad \Phi = \tfrac{\Phi'}{\gamma}, \quad \chi = 1, \\ &\qquad \eta \to \infty, \quad f' \to 0, \quad \theta \to 0, \quad \phi \to 0, \quad g' \to 0, \quad \Phi \to 0, \quad \chi \to 0 \end{aligned} \tag{25}$$

4 PINN (Physics Informed Neural Network)

4.1 PINN Structural Design

The neural network structure utilized in this work is a fully connected network (FCN) comprising an input layer, output layer and hidden layers, which together process input data to create a prediction. The architecture allows the network to receive input data, process nonlinear interactions through hidden layers, and produce desired output approximations. In the present study, the one-dimensional computational domain of the similarity variable η is divided into discrete nodes extending from 0 to η_∞. As shown in Fig. 2, boundary nodes are used to impose prescribed boundary conditions, whereas collocation nodes are distributed across the domain to satisfy the governing equations through the minimization of their residuals.

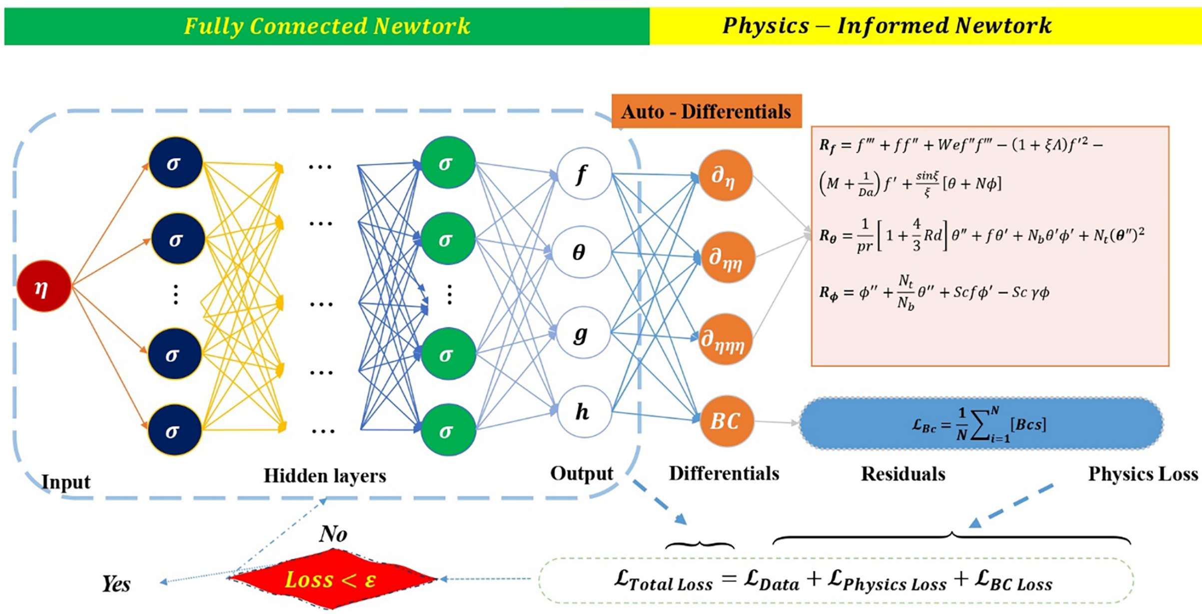

Figure 2: Flow chart representation of PINNs.

The input layer accepts the values of η_i while the output layer returns the predicted quantities $\widehat{y_i} = [f(\eta_i), \theta(\eta_i), \phi(\eta_i)]$. Information flows forward through the network as

$$z_i = b_i + \left(\sum_{j=1}^{j=n} a_j . w_{i,j}^{k} \right) \tag{26}$$

where w_{ij} and b_{ij} represent the weights and biases, respectively. A tanh activation function is utilized to add nonlinearity and increase expressiveness in the model. The loss function measures the difference between the network output and the real data, commonly via the mean squared error:

$$\text{Loss} = \frac{\left[\sum_{i=0}^{i=m} (y_i - \widehat{y_i})^2 \right]}{m} \tag{27}$$

4.2 Physics-Based Loss Function and Training Strategy

The data flows in a forward direction from one neuron to the next to calculate the output z_i. The process is continued layer by layer until the value of the estimated $\widehat{y_i}$ is calculated. As the process is initiated from assumed weight and bias values so it is assumed to observe significant deviation between the $\widehat{y_i}$ and y_i. It is necessary to set the weights and biases so that the calculated loss function decreased. This is done by utilizing the backpropagation approach and the chain rule to evaluate gradients of the loss with respect to the network parameters. These updates are made by using the Adam optimizer. The optimization process is carried out until the network has learnt the patterns available in the data sufficiently and the loss function meets the given convergence criteria. Raissi et al. [27] described a paradigm for constructing loss functions using ODEs. The loss measures the extent to which the expected outputs $\widehat{y_i}$ satisfy the underlying physical principles.

To reduce the loss function, the Adam optimizer iteratively updates weights and biases based on gradients computed via backpropagation. In the physics-based component, residual functions corresponding to the Physical Equations are embedded within the loss function as:

$$R_f = f''' + ff'' + Wef''f''' - (1 + \xi\Lambda) f'^2 - \left(M + \frac{1}{Da}\right) f' + \frac{sin\xi}{\xi}[\theta + N\phi] \tag{28}$$

$$R_\theta = \frac{1}{pr}\left[1 + \frac{4}{3}Rd\right]\theta'' + f\theta' + N_b\theta'\phi' + N_t(\theta')^2 + Ec(f'')^2 \tag{29}$$

$$R_\phi = \phi'' + \frac{N_t}{N_b}\theta'' + Scf\phi' - Sc\ K_r\phi \tag{30}$$

$$L_{physics} = \frac{1}{N}\sum_{i=1}^{N}(R_f^2 + R_\phi^2 + R_\theta^2) \tag{31}$$

Boundary conditions loss can be defined as:

$$L_{BC} = \frac{1}{N}\sum_{i=1}^{N}[f'(0)^2 + \left(\theta(0) - (1 + \frac{\theta'(0)}{\gamma})\right)^2 + f(0)^2 + (\phi(0) - 1)^2 + f'(\infty)^2 + \theta(\infty)^2 + \phi(\infty)^2] \tag{32}$$

The total loss function is defined as the weighted sum of physics loss and boundary condition loss

$$L_{total} = L_{phyiscs} + \lambda L_{BC} \tag{33}$$

where λ is the weighting coefficient assigned to the boundary condition loss.

Convergence of the proposed PINN is accomplished through the iterative minimization of loss function via Adam optimizer. With the reduction in total, physics and boundary condition losses are concurrently minimized to allow for the convergence of the network to solution that solves the governing equations and satisfies the boundary conditions.

4.3 Computational Implementation of the PINN

In the present study, a fully connected feed forward neural network architecture is used in order to simulate the coupled fluid flow, heat transfer and mass transport characteristics of a non-Newtonian Williamson fluid. The architecture consists of six hidden layers with sixty-two neurons and is trained with a learning rate of 5×10^{-4}. The hyperbolic tangent function, is utilized due to its smoothness and suitability for capturing nonlinear behavior inherent in boundary-layer problems. In all simulations, 300 collocation points were used, which were equally spaced in the domain $0 \le \eta \le 12$, whereas boundary conditions were prescribed at $\eta = 0$ and $\eta = 12$. The model weights were initialized randomly according to the default PyTorch weight initialization policy, while optimization was performed via the Adam optimizer with 5×10^{-4} an initial learning rate. The overall loss function is demarcated as the sum of the physics and B.Cs loss weighted by 0.01. Such a choice of the weighting coefficient guarantees stable convergence and the correct satisfaction of the governing equations and boundary conditions. All the computations have been carried out in the PyTorch framework by using its autograd module for accurate computation of the required derivatives for the imposition of the governing physics-based constraints. The proposed PINN model was developed within Python 3 programming language employing the PyTorch framework for deep learning and ran on the Google Colab cloud-based platform. The development process involved several free scientific computing packages such as NumPy library for numeric operations, PyTorch for building neural networks and automatic differentiation, SciPy for numerical verification and interpolation and Matplotlib for visualization of the simulation results. The computational simulations were conducted within a Python 3 environment offered by Google Colab using its computational resources.

5 Results and Discussions

5.1 Validation of the PINN Model

The governing equations of the current problem form a system of non-similar PDEs, as given by Eqs. (7)–(10), along with the boundary conditions specified in Eq. (11), are reduced to an ODEs system by the LNS approach, utilizing first and second-level truncations, as shown in Eqs. (19)–(24). The obtained nonlinear ODE system is finally solved by the PINNs approach. The network predictions are initially evaluated at 100 iterations, as depicted in Fig. 3a–c. At this point, there is a considerable difference between the predictions of the PINN and the numerical solution. With an increase in training epochs to 12,000, as shown in Fig. 4a–c, the predictions exhibit improved agreement, confirming the accuracy and robustness of the proposed approach. Express the L^2 error comparison between the numerical and PINN solutions (Table 1). The results demonstrate that increasing the number of iterations and training steps leads to a consistent reduction in L^2 error, showing better accuracy of the PINN framework.

The evolution of physic, boundary and total loss, which integrates machine learning with physics based terms, is illustrated in Fig. 5a–c, showing a consistent decline and stabilization as training progresses. The results show that there is high consistency of the PINN outputs and the numerical results, establishing the reliability and consistency between the developed PINN methodology for solving complex non-similar flow and heat transfer problems.

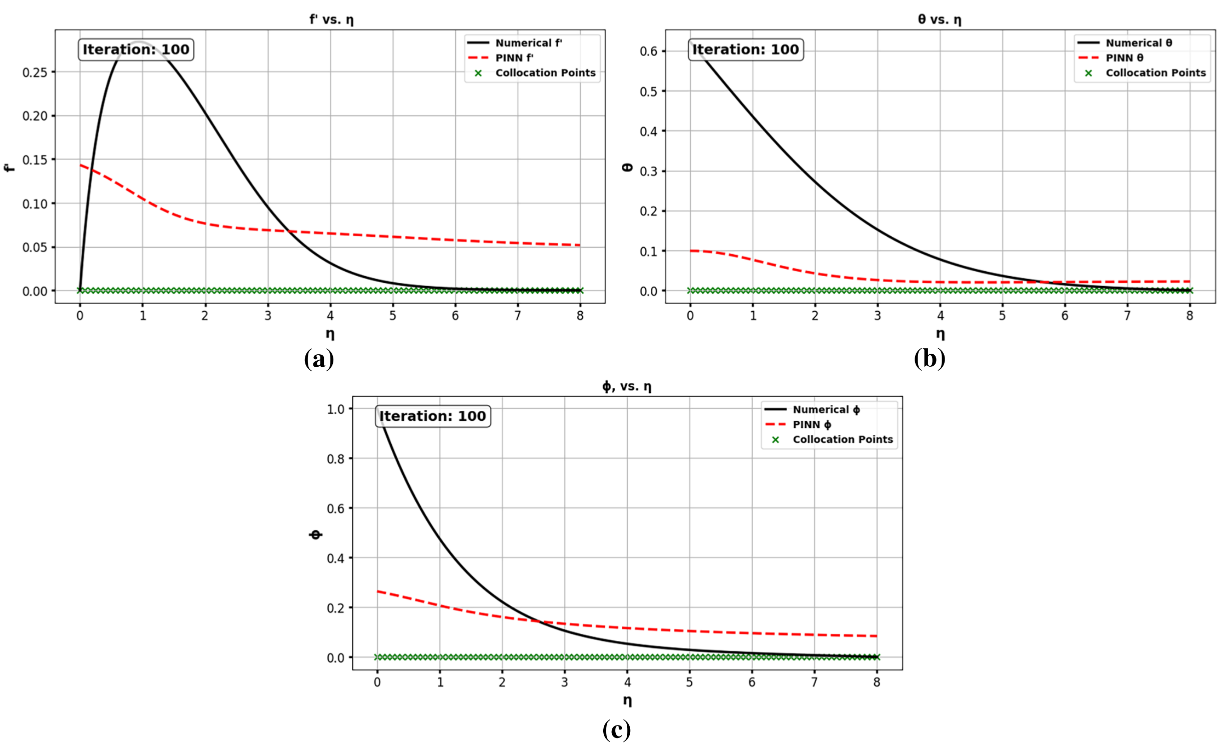

Figure 3: PINN vs. numerical solution with 100 epochs.

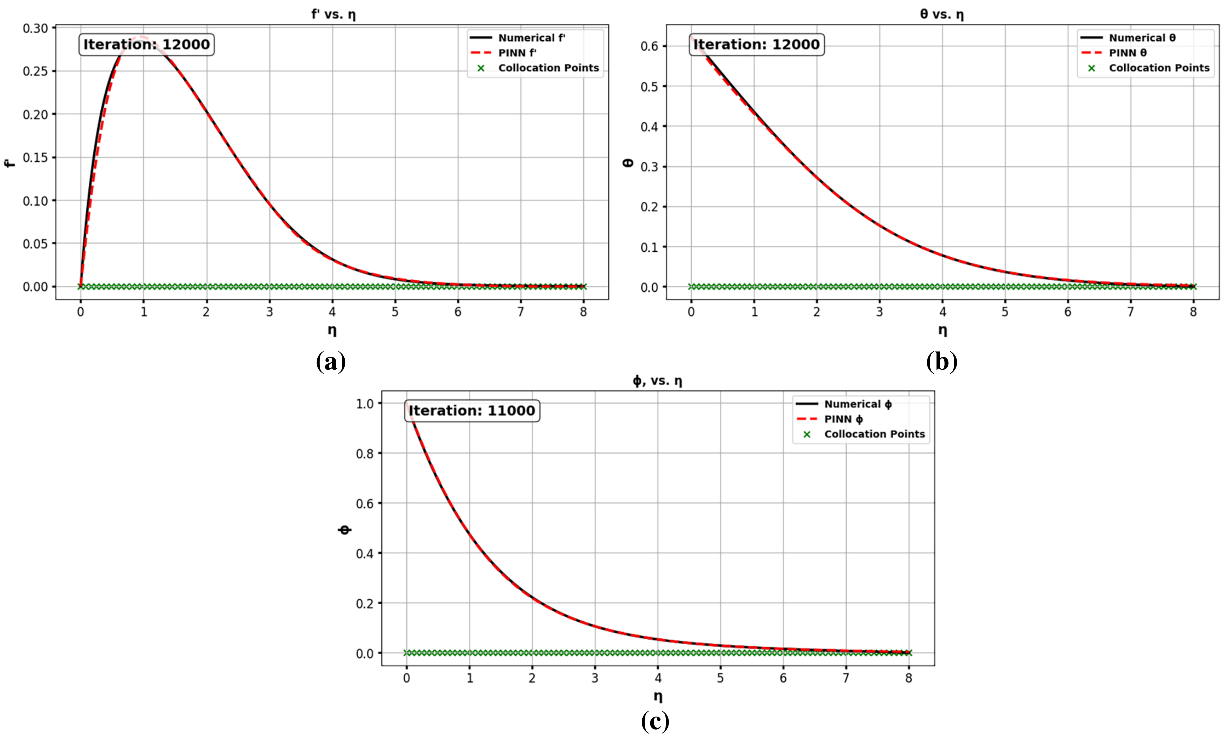

Figure 4: PINN vs. numerical solution with 12,000 epochs.

Table 1: L^2 error for different number of iterations.

Index	Iteration	L2 Error
0	100	0.261781
10	1100	0.037857
20	2100	0.025685
30	3100	0.018819
40	4100	0.014563
50	5100	0.011541
60	6100	0.009082
70	7100	0.006378
80	8100	0.004080
90	9100	0.003542
100	10,100	0.003506
110	11,000	0.003440
120	12,000	0.003400

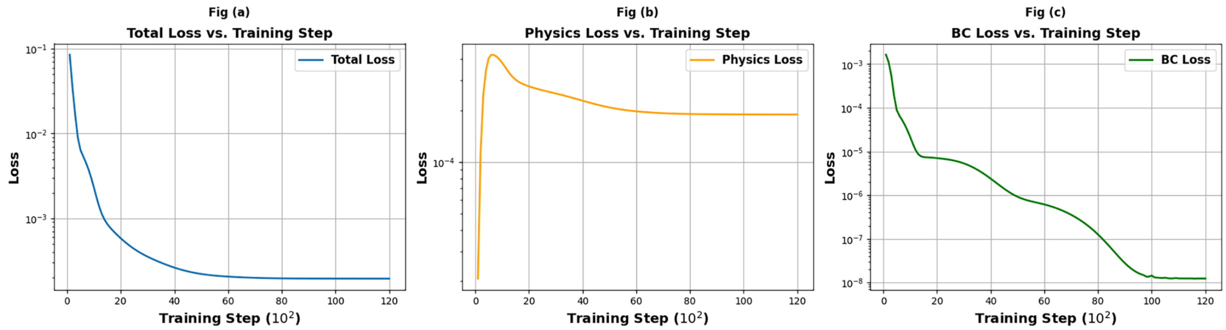

Figure 5: Total and physics loss convergence during training.

5.2 Parametric Analysis of Velocity, Temperature, and Concentration Profiles

The effect of the magnetic parameter M on the flow behavior is shown in Fig. 6a. The velocity profile decreases with increasing magnetic field intensity. This reduction is caused by the Lorentz force generated from the interaction between the external magnetic field and the electrically conducting Williamson nanofluid. Since the resultant force acts opposite to the direction of fluid motion, it introduces additional flow resistance and suppresses the momentum transport. The corresponding effects of M on the thermal field is represented in Fig. 6b as the magnetic field intensity rises, thermal profiles exhibit significant enhancement. Physically, the Lorentz force suppresses the fluid motion, reducing convective transport and allowing more time for thermal and solutal energy diffusion within the boundary layer. Consequently, this leads to a thicker thermal layer thus elevating the temperature near the surface. It is also clear from Fig. 6a,b that the predictions of the PINN match well with the numerical (SciPy) results for all values of M used in the study, proving the precision and effectiveness of the suggested model. In addition, the quantitative results shown in Table 2 indicates that the calculated L^2 errors are reasonably low for all values of M. Furthermore, the convergence characteristics of the proposed PINN framework are presented in Fig. 7. The monotonic and uniform decay of the total loss function for different values of M highlights the robustness, stability, and reliability of the PINN framework in capturing the highly nonlinear behavior of MHD boundary layer flow.

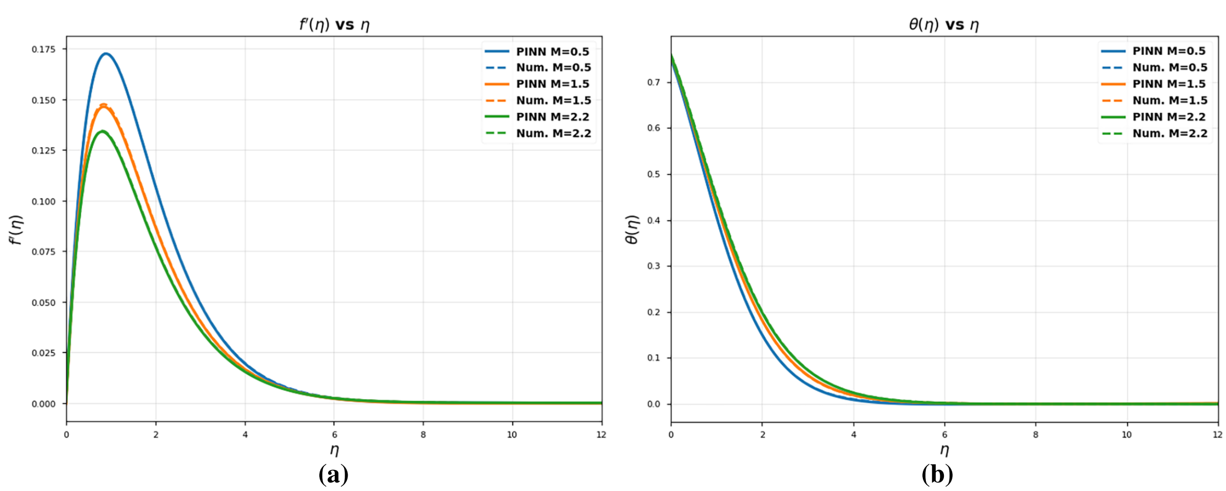

Figure 6: Velocity, temperature and profile for varying parameter M.

Table 2: L^2 error for variation of M.

M	$f'(\eta)$	$\theta(\eta)$	$\phi(\eta)$
0.5	1.04E−04	1.35E−03	1.16E−03
1.5	8.44E−03	2.20E−03	4.83E−03
2.2	7.46E−04	5.30E−04	9.16E−04

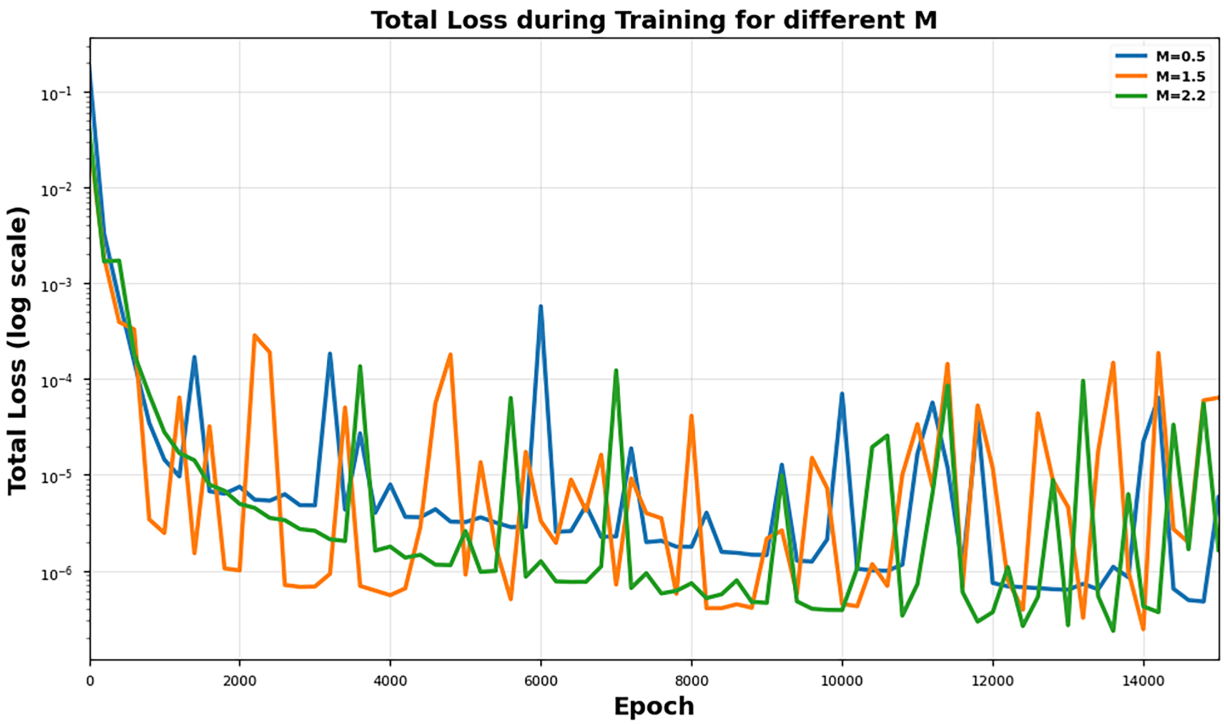

Figure 7: Total loss during training for varying M.

The Influence of the Prandtl number Pr on the flow, temperature, and concentration profiles is depicted in Fig. 8a–c. The increase in the Prandtl number is observed to result in a considerable reduction in the fluid velocity, temperature and concentration distributions. An increase in Prandtl numbercorresponds to lower thermal diffusivity, which suppresses heat diffusion and thereby decreases the temperature profile. Consequently, the reduced thermal buoyancy weakens the fluid motion, while the coupled heat and mass transfer mechanism leads to a slight reduction in the concentration distribution. It can be seen from these figures that the results of proposed PINN framework match the numerical solutions within the entire domain and hence reflect the highly accurate predictive capability of the proposed framework. To provide further quantitative evidence for such excellent agreement, the L^2 error values have been provided in Table 3. Moreover, the convergence behavior of the proposed PINN framework has been shown in Fig. 9. It can be observed from the evolution of the total loss function with respect to iterations that the total loss monotonically decreases with iterations. This indicates the highly stable and convergent nature of the proposed PINN framework under the constraint of governing equations, and boundary conditions. Parametric study of the Prandtl number holds great practical significance since it represents the relative magnitude of momentum and thermal diffusion. Such analyses are highly relevant to the design and optimization of heat exchangers, thermal energy storage systems, cooling of electronic devices, polymer processing, nuclear cooling systems, and other advanced thermal management technologies involving non-Newtonian nanofluids.

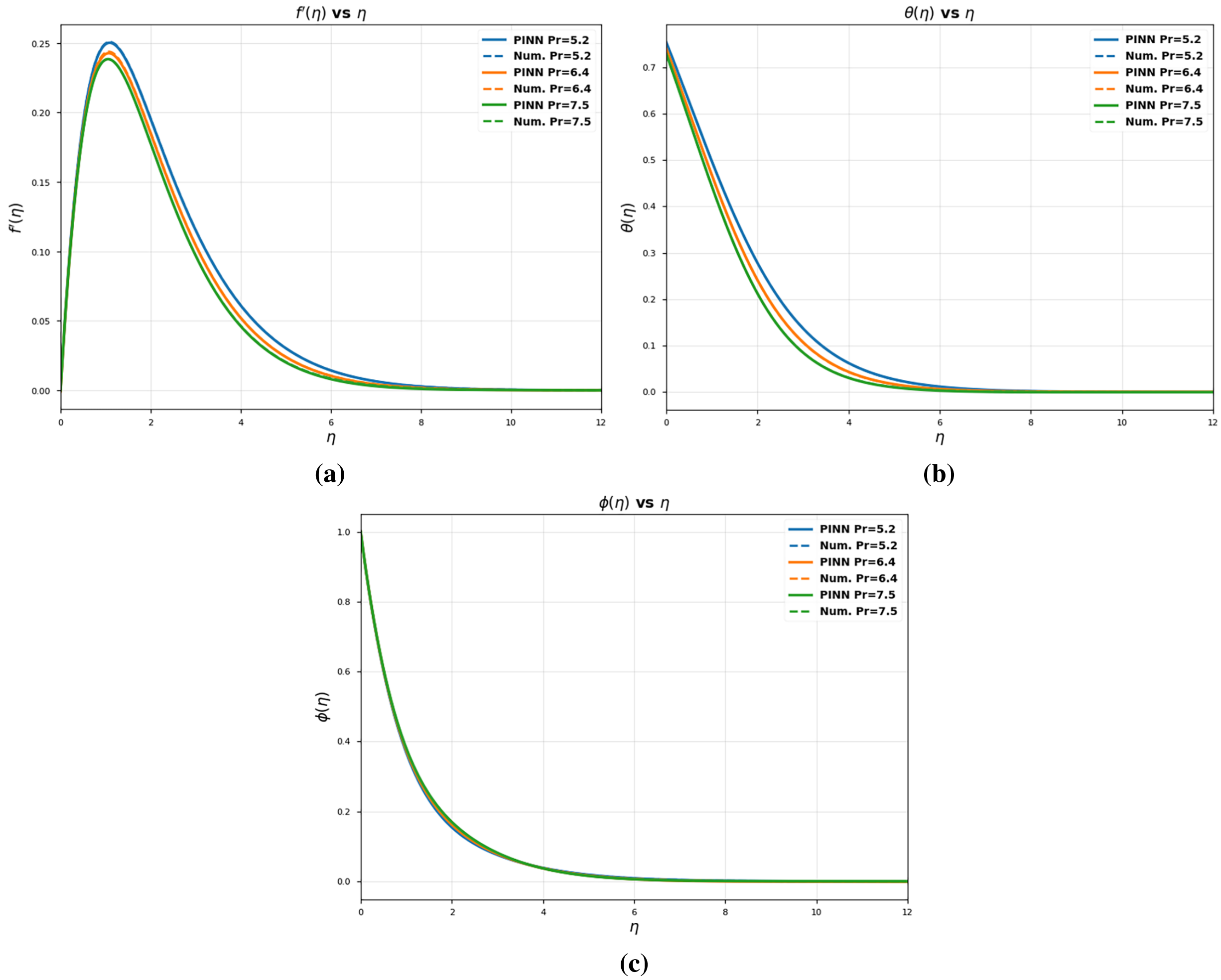

Figure 8: Velocity, temperature and concentration profile for varying parameter Pr.

Table 3: L^2 error for various value of Pr.

Pr	$f'(\eta)$	$\theta(\eta)$	$\phi(\eta)$
5.2	9.28E−03	2.69E−04	5.21E−03
6.4	9.05E−03	2.13E−04	4.32E−04
7.6	8.87E−03	4.36E−04	1.60E−03

The influence of the dimensionless heating parameter on velocity, temperature, and concentration distributions is demonstrated in Fig. 10a–c. As indicated by Fig. 10a, a rise in γ results in a significant decrease in velocity profile, which signifies that stronger surface heating increases resistance to fluid motion along the boundary, thus reducing the hydrodynamic layer. The effect of γ on the temperature field, shown in Fig. 10b, shows a higher thermal profile with higher γ. As the value of the convective heating parameter upturns, heat transfer coefficient at the cylinder surface becomes larger. Consequently, more thermal energy is transferred from the hot fluid surrounding the cylinder to the nanofluid within the boundary layer. This enhanced convective heat exchange raises the fluid temperature, resulting in a thicker thermal boundary layer and an increase in $\theta(\eta)$ profile. The concentration profile in Fig. 10c decreases as γ increases. This behavior is attributed to the coupled heat and mass transfer mechanism, resulting in a thinner concentration boundary layer. In addition, the convergence behavior of the PINN model is shown in Fig. 11, illustrating the variation of the total loss function during training of the model. The monotonically decreasing trend of total loss with the increase in iterations and network depth validates the stability, precision, and excellent generalization ability of the constructed PINN model in modeling the underlying coupled flow, and transport phenomenon.

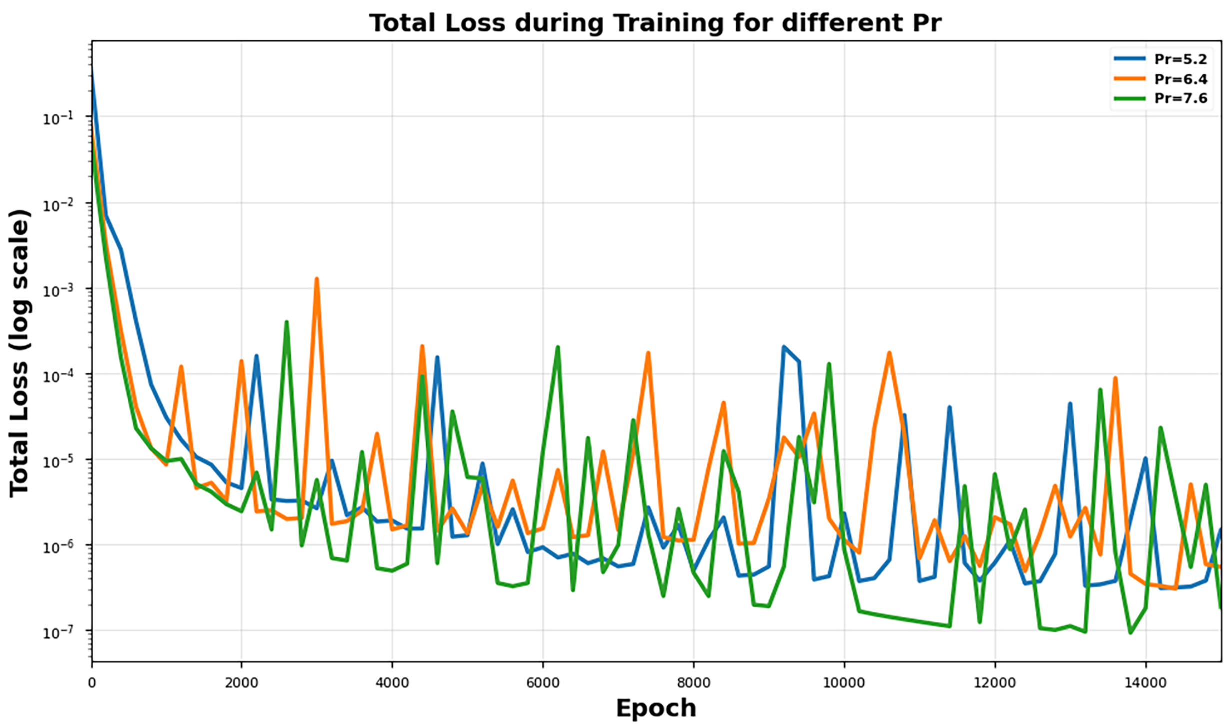

Figure 9: Total loss during training for varying Pr.

The upshot of the Schmidt number Sc on flow behavior is shown in Fig. 12a–c. From Fig. 12a, the velocity profile is reduced with increasing Sc, meaning that larger values of the Schmidt number, corresponding to stronger momentum diffusivity compared to mass diffusivity, restrain fluid movement in the boundary layer. Similarly, the temperature distribution is given by Fig. 12b, increasing slightly with growing Sc. From a physical perspective, the upturn in the value of the Schmidt number is associated with the decrease in mass diffusivity of the nanoparticles, and thus it inhibits the diffusion of particles within the boundary layer. For this reason, the existence of nanoparticles within the fluid becomes longer and the effectiveness of the coupled heat transfer process via Brownian motion and thermophoresis increases. Thus, the process of heat accumulation takes place, which causes the growth of the thermal boundary layer thickness and the fluid temperature. The associated concentration profile depicted in Fig. 12c also shows a smooth decrease with Sc increasing. This is because high Schmidt numbers are associated with fluids having low molecular diffusivity, thus decreasing the species transport rate and leading to a lower concentration boundary layer thickness. In addition, the convergence history of PINN model is shown in Fig. 13; the monotonic and regular decrease in the loss function ensures the good learning capability of the PINN model in approximating the coupled nonlinear transport processes of momentum, heat, and mass transfer with high precision and stability.

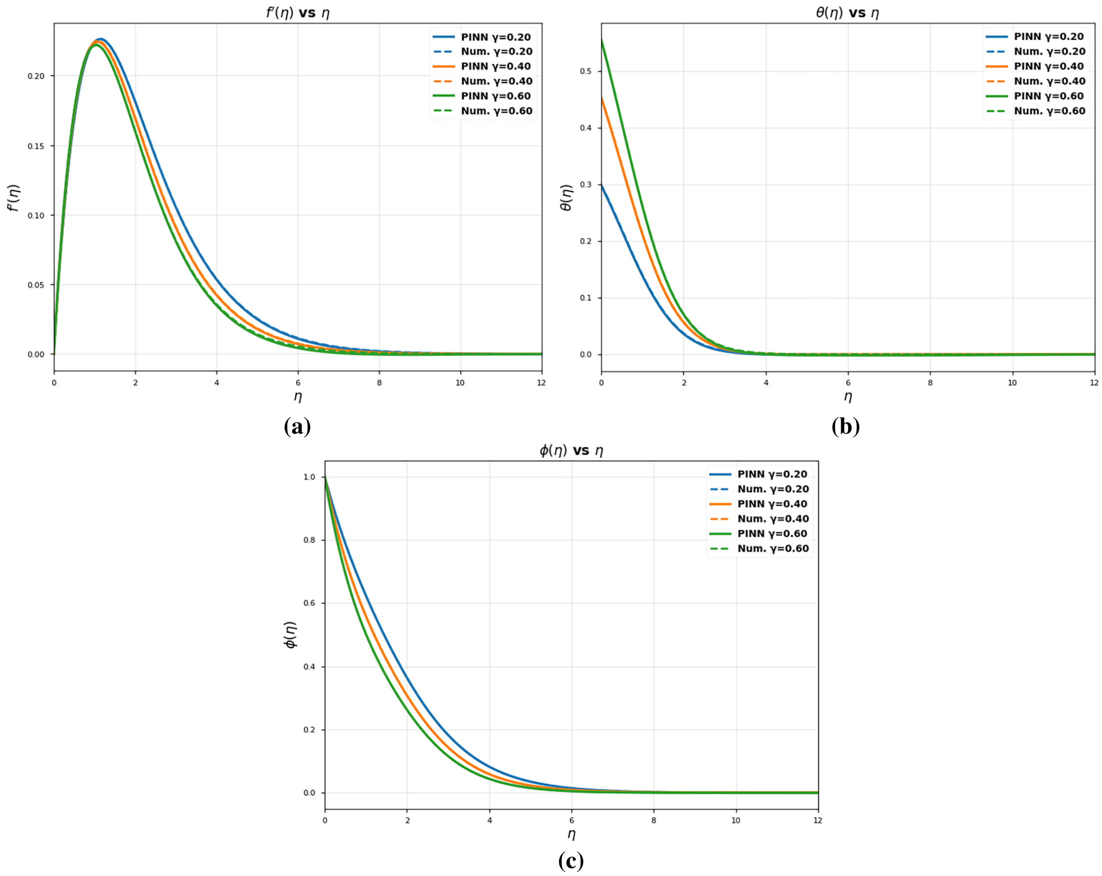

Figure 10: Impact of γ on velocity, temperature and concentration parameter.

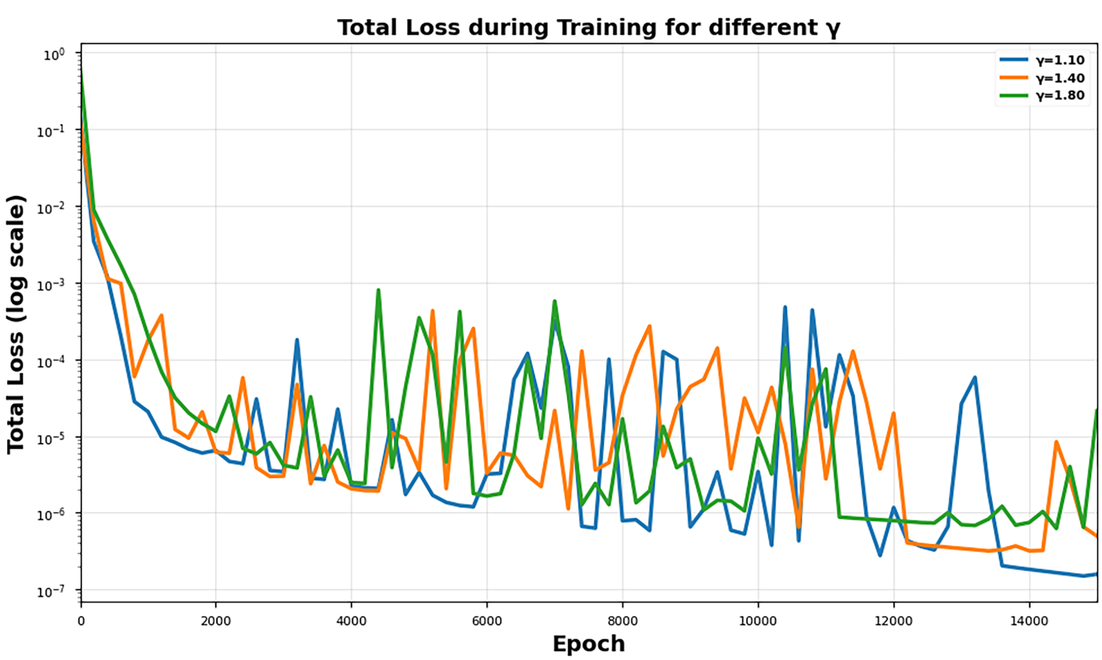

Figure 11: Total loss during training for varying γ.

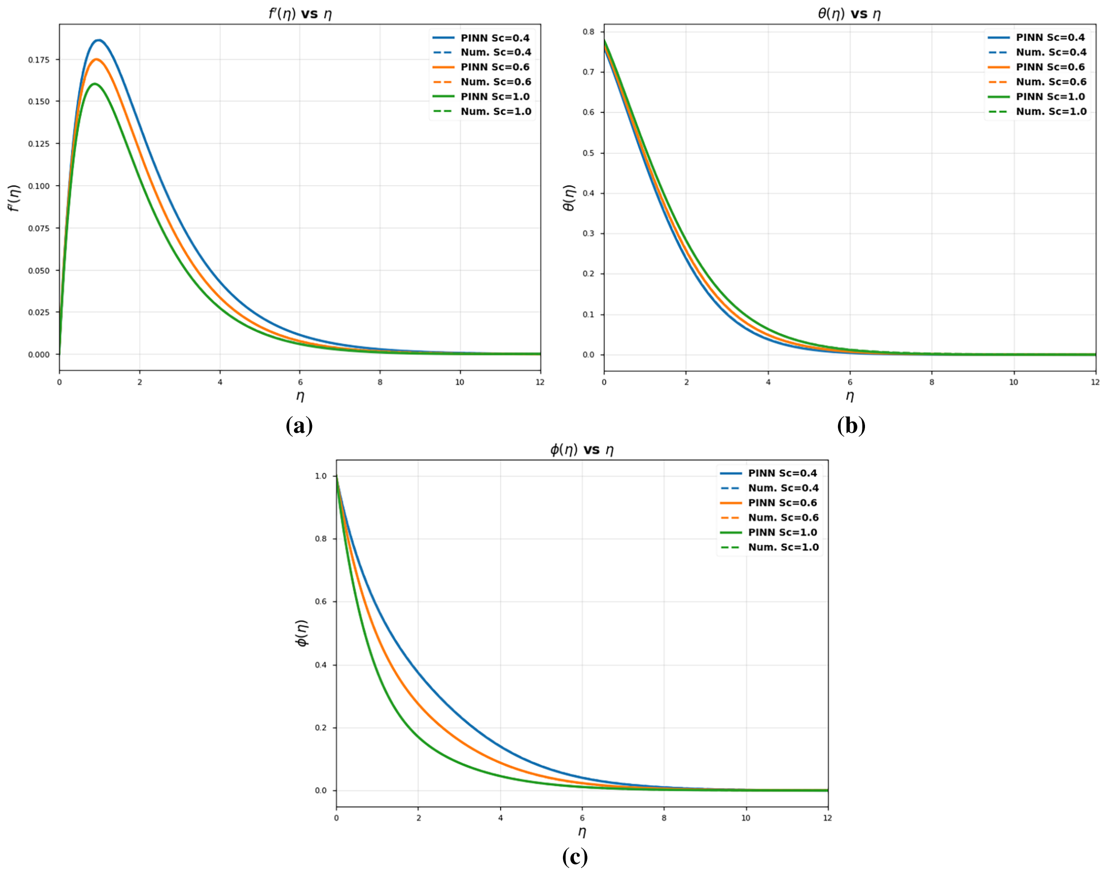

Figure 12: Effect of Sc on velocity, temperature and concentration profile.

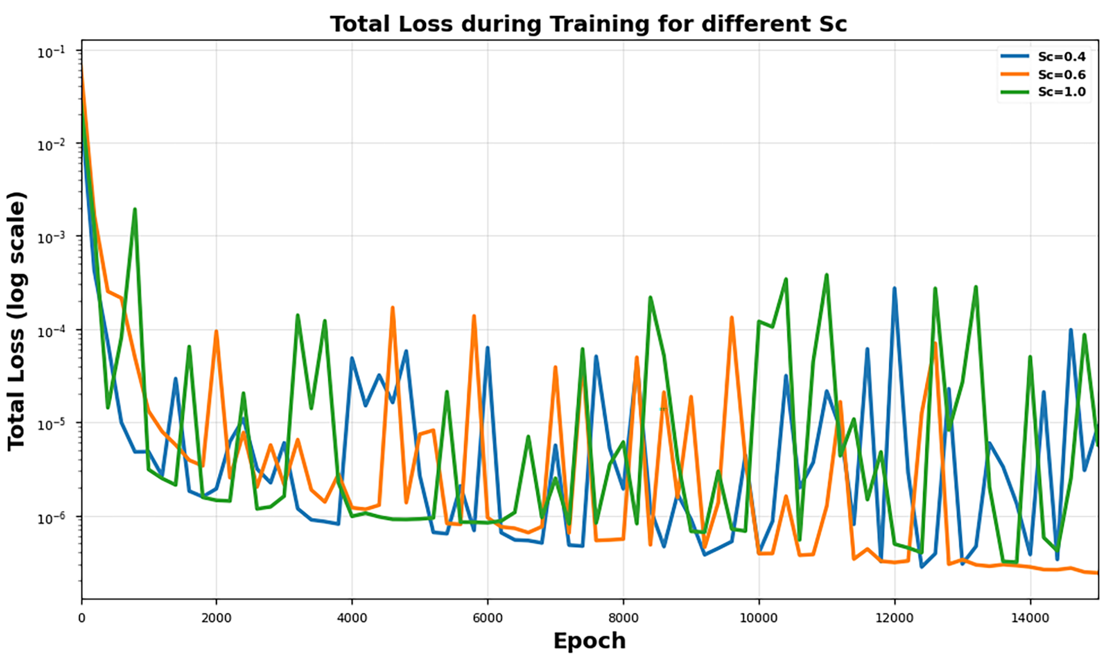

Figure 13: Total loss during training for varying Sc.

In Figs. 10 and 12, the dashed curves indicate the numerical results while the solid lines indicate the PINN solutions. It is clear from the figures that the PINN results exhibit strong agreement with the reference solutions over the entire computational domain, thereby validating the high accuracy and reliability of the proposed approach. To measure the extent of agreement between the two approaches, L^2 error norms corresponding to various γ and Sc are provided in Tables 4 and 5, respectively. The small values of L^2 error norms further validate the high agreement between the two approaches and the robustness and predictive capabilities of the proposed approach. The analysis of the convection heating parameter and Schmidt number is highly important in many real world engineering problems related to the coupled heat and mass transfer phenomena such as heat exchangers, polymer processing, drying, chemical reactors, porous medium transport, membrane separation and biomedical systems.

Table 4: L^2 error for variation of γ.

γ	$f'(\eta)$	$\theta(\eta)$	$\phi(\eta)$
1.1	1.04E−04	3.32E−06	2.98E−04
1.4	1.01E−05	6.71E−04	2.91E−04
1.8	9.88E−04	1.05E−03	9.92E−04

Table 5: Evaluation of L^2 error for variation of Sc.

Sc	$f'(\eta)$	$\theta(\eta)$	$\phi(\eta)$
0.4	1.16E−03	4.81E−04	2.24E−03
0.6	1.08E−02	1.03E−04	1.43E−04
1	9.77E−04	7.21E−04	1.36E−03

5.3 Influence of Physical Parameters on Surface Transport Quantities

The contour plots in Fig. 14 illustrate the variation of the skin friction coefficient with different thermo-physical parameters. The skin friction coefficient decreases with increasing Pr, whereas it increases slightly with increasing N_b. The reduction in skin friction with increasing Pr is associated with the suppression of fluid velocity near the cylinder surface, leading to a lower wall shear stress. In contrast, increasing N_b slightly enhances the wall shear stress, resulting in a marginal increase in the skin friction coefficient. Fig. 15 illustrates convective heat transfer rate at the cylinder surface. The results demonstrates, rising the Prandtl number or N_b upsurges the Nusselt number, reflecting increased convective heat transfer as a result of higher thermal gradients in the vicinity of the surface. Fig. 16 show the Sherwood number behavior, the mass transfer rate at the fluid–solid interface. The contour of Pr-N_b shows the amassed Pr, a decreasing Sh by a slight extent and the increase in N_b increasing it further, indicating better nanoparticle diffusion to the surface. These findings have significant physical ramifications for applications involving mass and thermal transportation. For instance, heat and mass transfer in nanofluid-based cooling systems, chemical reactors, or microelectronics can be optimized by increasing Brownian motion or modifying the Prandtl number. The results show that adjusting these variables enables more effective surface cooling and focused nanoparticle deposition, which can be customized to enhance performance in engineering and industrial applications.

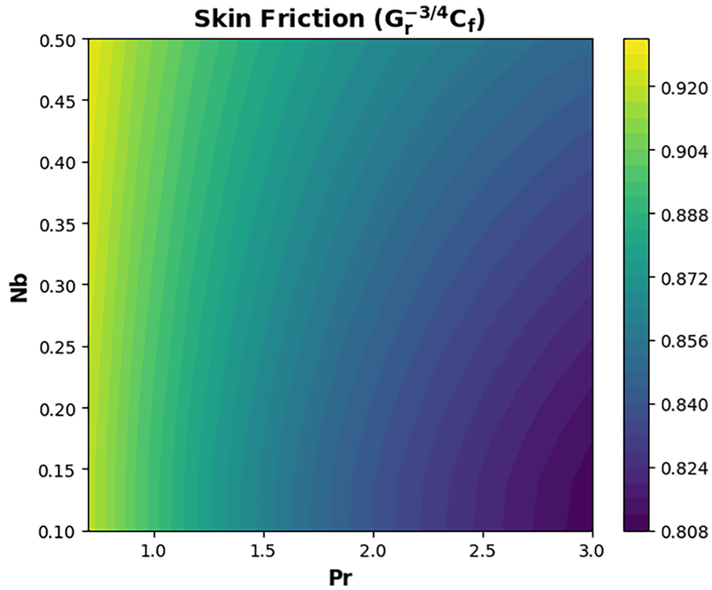

Figure 14: Skin friction coefficient of N_b and Pr.

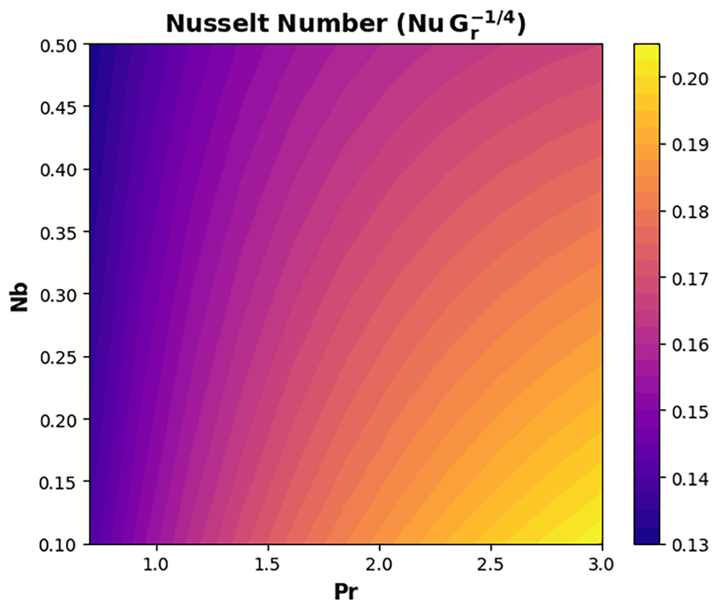

Figure 15: Nusselt number coefficient of N_b and Pr.

The effect of the thermophysical parameter N_t and Schmidt number Sc reveals that the enhancement of N_t decreases skin friction slightly, whereas larger Sc enhances viscous effects, thus increasing wall shear stress as depicted in Fig. 17. The trends of the above dependences reveal the predominance of momentum diffusion and viscous drag in Williamson fluid under the impact of magnetic and porous medium effects. Fig. 18 shows the effect of ruling parameters on local Nusselt number, which defines the rate of heat transfer on the cylinder surface. The research shows that a steady decrease in Nu is observed as N_t increases, indicating that excess thermophoretic motion inhibits temperature gradients by redistributing thermal energy from the wall. The global trends verify that heat transfer in the Williamson fluid is greatly influenced by both mechanisms of nanoparticle diffusion and thermal conductivity variation within the porous medium. Fig. 19 illustrates that a rise in Schmidt number corresponds to a considerable increase in Sh, suggesting greater resistance to mass diffusion due to lower molecular diffusivity. As an alternative, raising N_t lowers Sh, demonstrating that greater thermophoretic movement tends to expel species away from the wall. These findings highlight the coupled effect of heat and mass diffusion on magnetized Williamson fluid flow in a porous medium. It is clear from the results that increasing the thermophoretic parameter diminishes heat and mass transfer at the cylinder surface, while larger Schmidt numbers increase wall shear stress and enhance mass accumulation. These specific effects hint that in cases of applications like nanofluid-based cooling or porous structure drug delivery, tuning N_t and Sc directly serves to control the transportation of mass and heat in magnetized flows. Furthermore, Table 6 presents a comparison of the present results with the benchmark results available in the literature, demonstrating excellent agreement and thereby confirming the accuracy and reliability of the proposed computational framework. The results of this investigation offer valuable recommendations for the development and enhancement of advanced engineering systems like nanofluid heat exchangers, electronic coolers, solar thermal collectors, polymeric processing, porous catalytic reactors, membrane separators, geothermal systems and biomedical transport phenomena such as targeted drug delivery.

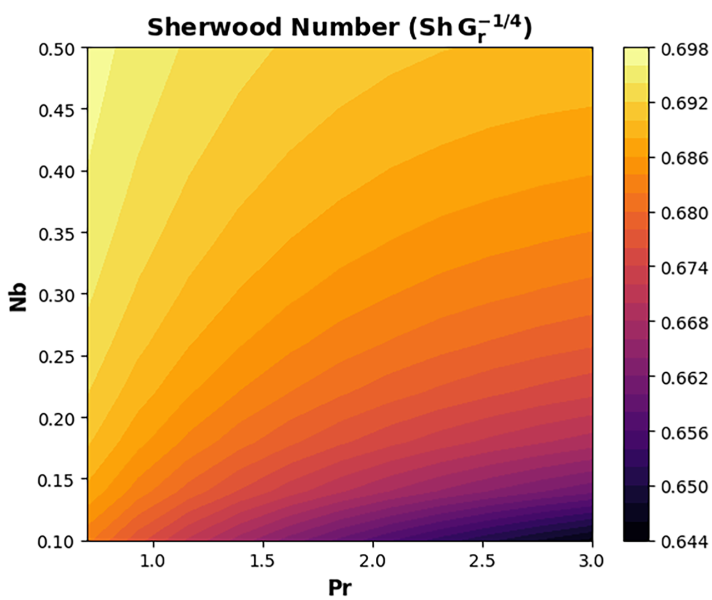

Figure 16: Sherwood number coefficient of N_b and Pr.

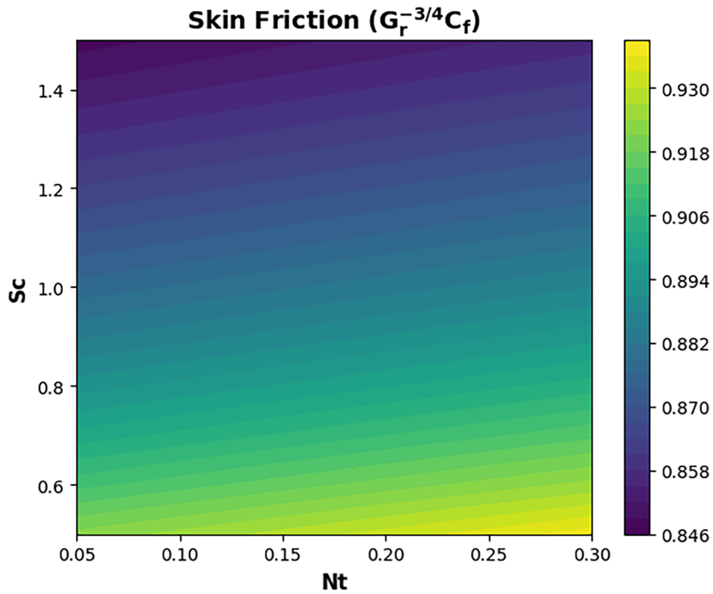

Figure 17: Skin friction coefficient of N_t and Sc.

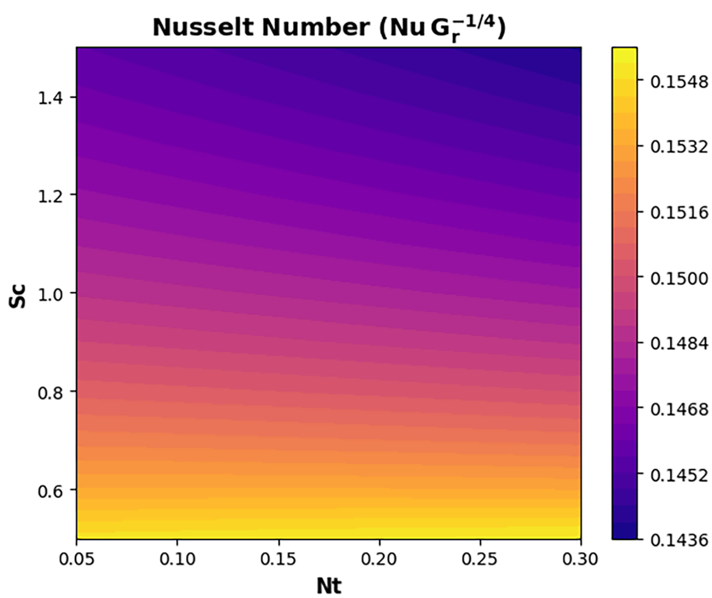

Figure 18: Nusselt number coefficient of N_t and Sc.

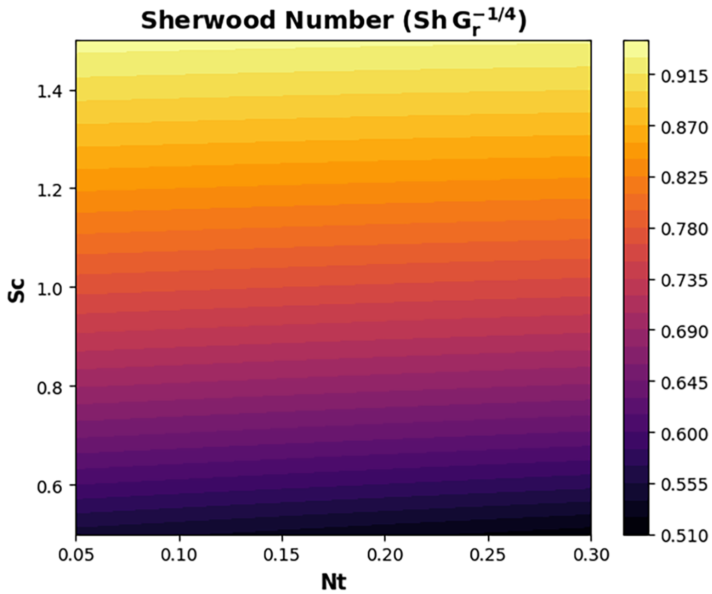

Figure 19: Sherwood number coefficient of N_t and Sc.

Table 6: Comparison of the present results with existing numerical findings.

We	C_f**Subba Rao et al. [24]**	C_f**Current Results**
0.00	0.4136	0.4125
0.30	0.4176	0.4174
0.50	0.4201	0.4202
0.80	0.4239	0.4237
1.00	0.4261	0.4254
1.50	0.4316	0.4314
2.00	0.4367	0.4364

6 Conclusion and Future Work

The present work introduces a hybrid computational framework that combines the LNS approach with PINN to analyze the non-similar boundary layer flow, heat transfer, and mass transport of a Williamson nanofluid over a horizontal cylinder. The developed PINN embeds the transformed governing equations together with the associated boundary conditions directly into a physics-guided loss function, ensuring that the learned solution satisfies the underlying physical laws. The obtained PINN model predictions demonstrate excellent consistency with benchmark numerical solutions, indicating the accuracy and effectiveness of the proposed LNS–PINN methodology for simulating complex nonlinear transport phenomena.

The major conclusions drawn from the present investigation are summarized as follows:

❖ The proposed LNS-PINN technique efficiently simulates the non-similar Williamson nanofluid flow problem with good accuracy by showing good consistency with the numerical solution obtained by the Scipy solver technique. The combination of the Local Non-Similarity concept and Physics-Informed Neural Networks offers an innovative method for computing strongly nonlinear transport phenomena without discretizing the domain.

- The enhancement in the value of the magnetic field parameter M leads to a decrease in fluid velocity and an increase in temperature distribution.
- The enhancement of the heat generation factor γ results in a lowering of the velocity profile, raising the thermal and decreasing the concentration profile.
- An increase in the Prandtl number causes a reduction in both the velocity profile and temperature profile. The higher Prandtl number has low values of thermal diffusivity, which inhibit the diffusion of thermal energy.
- The Schmidt number (Sc) enhances the temperature profile while reducing both the velocity profile and the concentration profile. High values of the Schmidt number result in decreased molecular diffusion of mass and thus reduced nanoparticle flow.
- The transport phenomena in engineering applications are highly dependent on the thermophysical variables of interest. The skin friction coefficient is lower for larger values of the Brownian motion parameter and Prandtl number but higher with the increment in Sc and is reduced slightly by the increase in the thermophoretic parameter.
- The local Nusselt number surges with growing Pr and N_b and shows enhanced convective heat transfer due to greater thermal gradients near the cylinder. However, with the increment in N_t, the Nu_x falls since the movement reduces the temperature gradient at the wall.
- The values of the local Sherwood number rise with growing Sc and N_b, and are decreased by the increase in the thermophoretic parameter.
- The results obtained in this work will undoubtedly serve as the key point for developing optimal solutions for nanofluids in applications of nanofluidic cooling, electronics thermal management, heat exchangers, porous energy systems, chemical reactions, biomedical applications, photovoltaics, metallurgy, magnetic transport, and so forth, where accurate simulation of transport processes is critical.

The current study is restricted to two-dimensional, steady, and laminar flow under the assumptions of negligible induced magnetic effect, local thermal equilibrium, and negligible Hall current effects. Furthermore, the proposed PINN framework is validated against benchmark numerical solutions rather than experimental measurements.

Future investigation may focus on:

- Extend the planned framework to unsteady and 3D flow problems.
- Apply the methodology to hybrid and multiphase nanofluids.
- Develop adaptive or domain-decomposition PINN frameworks to improve computational efficiency.
- Validate the proposed model using high-fidelity Computational Fluid Dynamics (CFD) simulations and experimental measurements.
- Extend the framework to inverse problems, parameter estimation, and turbulent transport phenomena.

Acknowledgement: This work was supported by Princess Nourah bint Abdulrahman University Researchers Supporting Project number (PNURSP2026R928), Princess Nourah bint Abdulrahman University, Riyadh and Saudi Arabia. The authors would like to express their sincere appreciation to Universiti Teknikal Malaysia Melaka (UTeM) for the facilities, support, and encouragement provided throughout this research work. This study was financially supported under the grant ANTARABANGSA(IRMG)-TEL-U/2025/FTKM/A00085.

Funding Statement: This work was funded by Princess Nourah bint Abdulrahman University Researchers Supporting Project number (PNURSP2026R928), Princess Nourah bint Abdulrahman University, Riyadh, Saudi Arabia. The authors would like to express their sincere appreciation to Universiti Teknikal Malaysia Melaka (UTeM) for the facilities, support, and encouragement provided throughout this research work. This study was financially supported under the grant ANTARABANGSA(IRMG)-TEL-U/2025/FTKM/A00085.

Author Contributions: Hameed Ullah Khan: PINN implementation, Data curation, Writing—original draft preparation and Manuscript revision. Muhammad Naveed Khan: Supervision, Conceptualization, Manuscript review and editing. N. Ameer Ahammad: Formal analysis, Validation, Manuscript review. Nurul Amira Zainal: Investigation, Funding acquisition, Project administration. Shahzad Sarwar: Supervision, Data analysis, Validation. Muhammad Imran Khan: Visualization, Software, Methodology. Afef Dhahbi: Critical review, Interpretation of results, Final approval of the manuscript. All authors reviewed and approved the final version of the manuscript.

Availability of Data and Materials: The datasets generated and analyzed during the current study are available from the corresponding authors upon reasonable request. All data presented in this study are original.

Ethics Approval: Not applicable.

Conflicts of Interest: The authors declare no conflicts of interest.

Nomenclature

Symbol	Description
B_0	Magnetic field
ξ	Dimensionless streamwise coordinate
Gr	Grashof number
g	Acceleration due to gravity
M	Magnetic body force parameter
Pr	Prandtl number
a	Radius of the cylinder
T	Temperature
We	Weissenberg number
C_f	Skin friction coefficient
x	Streamwise coordinate
Nu	Local Nusselt number
k	Thermal conductivity
C_∞	Ambient concentration
α	Thermal diffusivity
η	Dimensionless transverse coordinate
q_r	Radiative heat flux
ψ	Stream function
ϕ	Dimensionless concentration
C_w	Surface concentration
T_w	Surface temperature
σ^*	Stefan–Boltzmann constant
k^*	Mean absorption coefficient
h_w	Convective heat transfer coefficient
Da	Darcy number
N	Buoyancy ratio
N_t	Thermophoresis parameter
Ec	Eckert number
γ	Dimensionless heating parameter
θ	Dimensionless temperature
ρ	Density
Γ	Time-dependent material constant (relaxation parameter)
β_c	Solutal expansion coefficient
ν	Kinematic viscosity

β	Thermal expansion coefficient
c	inertial coefficient
K	Permeability of porous medium
y	Transverse coordinate
u, v	velocity components
T_∞	Ambient temperature
D_T	Thermophoretic diffusion coefficient
σ	Electrical conductivity
Rd	Thermal radiation parameter
Sh	Local Sherwood number
D_B	Mass diffusivity
K_1	Chemical reaction rate constant
c_p	Specific heat at constant pressure
ΔT	Temperature difference
N_b	Brownian motion parameter

Abbreviations

PINN	Physics Informed Neural Network
K_r	Chemical reaction parameter
ANN	Artificial Neural Network
LNS	Local non-similarity
MHD	Magnetohydrodynamics

References

1. Heaton H. Ian Goodfellow, Yoshua Bengio, and Aaron Courville: deep learning. Genet Program Evolvable Mach. 2018;19(1):305–7. doi:10.1007/s10710-017-9314-z.
2. Baydin AG, Pearlmutter BA, Radul AA, Siskind JM. Automatic differentiation in machine learning: a survey. J Mach Learn Res. 2017;18(1):5595–637. doi:10.5555/3122009.3242010.
3. Raissi M, Perdikaris P, Karniadakis GE. Physics-informed neural networks: a deep learning framework for solving forward and inverse problems involving nonlinear partial differential equations. J Comput Phys. 2019;378:686–707. doi:10.1016/j.jcp.2018.10.045.
4. Cai S, Mao Z, Wang Z, Yin M, Karniadakis GE. Physics-informed neural networks (PINNs) for fluid mechanics: a review. Acta Mech Sin. 2021;37(12):1727–38. doi:10.1007/s10409-021-01148-1.
5. Cai S, Wang Z, Wang S, Perdikaris P, Karniadakis GE. Physics-informed neural networks for heat transfer problems. J Heat Transf. 2021;143(6):060801. doi:10.1115/1.4050542.
6. Bararnia H, Esmaeilpour M. On the application of physics informed neural networks (PINN) to solve boundary layer thermal-fluid problems. Int Commun Heat Mass Transf. 2022;132(8):105890. doi:10.1016/j.icheatmasstransfer.2022.105890.
7. E. W, Yu B. The deep ritz method: a deep learning-based numerical algorithm for solving variational problems. Commun Math Stat. 2018;6(1):1–12. doi:10.1007/s40304-018-0127-z.
8. Ainsworth M, Dong J. Galerkin neural network approximation of singularly-perturbed elliptic systems. Comput Meth Appl Mech Eng. 2022;402(3):115169. doi:10.1016/j.cma.2022.115169.
9. Arzani A, Cassel KW, D'Souza RM. Theory-guided physics-informed neural networks for boundary layer problems with singular perturbation. J Comput Phys. 2023;473(3):111768. doi:10.1016/j.jcp.2022.111768.
10. Gie GM, Hong Y, Jung CY, Lee D. Singular layer physics-informed neural network method for convection-dominated boundary layer problems in two dimensions. arXiv:2312.03295. 2023.
11. Cong K, Li G, Sun Y, Ren H. Using physics-informed derivative networks to solve the forward problem of a free-convective boundary layer problem. Sci Rep. 2025;15(1):18766. doi:10.1038/s41598-025-03918-4.

12. Zeeshan A, Khalid N, Ellahi R, Khan MI, Alamri SZ. Analysis of nonlinear complex heat transfer MHD flow of Jeffrey nanofluid over an exponentially stretching sheet via three phase artificial intelligence and Machine Learning techniques. Chaos Solitons Fractals. 2024;189(1):115600. doi:10.1016/j.chaos.2024.115600.
13. Adekanmbi-Akinseye OA, Fenuga OJ, Isede HA, Sobamowo MG. Flow and heat transfer of a dusty williamson MHD nanofluid flow over a permeable cylinder in a porous medium. Open J Fluid Dyn. 2024;14(2):100–22. doi:10.4236/ojfd.2024.142005.
14. Zheng M, Khan MI, Khan HU, Hazim A, Zeeshan A, Ijaz N, et al. Mixed convection with boundary layer flow of hybrid nanofluid forchheimer effects via horizontal cylinder: intelligent exogenous networks. Multiscale Multidiscip Model Exp Des. 2025;8(8):348. doi:10.1007/s41939-025-00928-7.
15. Zaman SU, Aslam MN, Riaz MB, Akgul A, Hussan A. Williamson MHD nanofluid flow with radiation effects through slender cylinder. Results Eng. 2024;22(11):101966. doi:10.1016/j.rineng.2024.101966.
16. Rasool G, Chamkha AJ, Muhammad T, Shafiq A, Khan I. Darcy-Forchheimer relation in Casson type MHD nanofluid flow over non-linear stretching surface. Propuls Power Res. 2020;9(2):159–68. doi:10.1016/j.jppr.2020.04.003.
17. Gorla RS, Chamkha AJ, Rashad AM. Mixed convective boundary layer flow over a vertical wedge embedded in a porous medium saturated with a nanofluid: natural convection dominated regime. Nanoscale Res Lett. 2011;6(1):207. doi:10.1186/1556-276X-6-207.
18. Huang Y, Zhang Z, Zhang X. A direct-forcing immersed boundary method for incompressible flows based on physics-informed neural network. Fluids. 2022;7(2):56. doi:10.3390/fluids7020056.
19. Ang EHW, Wang G, Ng BF. Physics-informed neural networks for low Reynolds number flows over cylinder. Energies. 2023;16(12):4558. doi:10.3390/en16124558.
20. Dou Y, Han X, Lin P. Flow field reconstruction and prediction of the two-dimensional cylinder flow using data-driven physics-informed neural network combined with long short-term memory. Eng Appl Artif Intell. 2025;149(7):110547. doi:10.1016/j.engappai.2025.110547.
21. Zhu Y, Kong W, Deng J, Bian X. Physics-informed neural networks for incompressible flows with moving boundaries. Phys Fluids. 2024;36(1):013617. doi:10.1063/5.0186809.
22. Ren X, Hu P, Su H, Zhang F, Yu H. Physics-informed neural networks for transonic flow around a cylinder with high Reynolds number. Phys Fluids. 2024;36(3):200384. doi:10.1063/5.0200384.
23. Kim J, Khan HU, Imran Khan M, Asghar Z, Zeeshan A. Physics-informed neural networks for heat transfer in non-Newtonian Casson fluid flow around a horizontal cylinder. Int J Comput Meth Eng Sci Mech. 2026;27(1):54–67. doi:10.1080/15502287.2025.2606706.
24. Subba R A, Amanulla CH, Nagendra N, Anwar Bég O, Kadir A. Hydromagnetic flow and heat transfer in a williamson non-Newtonian fluid from a horizontal circular cylinder with Newtonian heating. Int J Appl Comput Math. 2017;3(4):3389–409. doi:10.1007/s40819-017-0304-x.
25. Minkowycz WJ, Sparrow EM. Numerical solution scheme for local nonsimilarity boundary-layer analysis. Numer Heat Transf Part B Fundam. 1978;1(1):69–85. doi:10.1080/10407797809412161.
26. Sparrow EM, Abraham JP. Universal solutions for the streamwise variation of the temperature of a moving sheet in the presence of a moving fluid. Int J Heat Mass Transf. 2005;48(15):3047–56. doi:10.1016/j.ijheatmasstransfer.2005.02.028.
27. Raissi M, Perdikaris P, Karniadakis GE. Physics informed deep learning (part I): data-driven solutions of nonlinear partial differential equations. arXiv:1711.10561. 2017.